



# Thread-structural microneedles loaded with engineered exosomes for annulus fibrosus repair by regulating mitophagy recovery and extracellular matrix homeostasis

Shaojun Hu<sup>a,b,c,d,1</sup>, Meng Zhu<sup>e,1</sup>, Hongyuan Xing<sup>f</sup>, Yucheng Xue<sup>a,b,c,d</sup>, Jun Li<sup>a,b,c,d</sup>, Zhan Wang<sup>a,b,c,d</sup>, Zhou Zhu<sup>e</sup>, Miaojie Fang<sup>a,b,c,d</sup>, Zilong Li<sup>a,b,c,d</sup>, Jianbin Xu<sup>a,b,c,d,\*</sup>, Yong He<sup>e,\*\*</sup>, Ning Zhang<sup>a,b,c,d,\*\*\*</sup>

<sup>a</sup> Department of Orthopedic Surgery, The Second Affiliated Hospital, Zhejiang University School of Medicine, Hangzhou City, Zhejiang Province, PR China

<sup>b</sup> Orthopedics Research Institute of Zhejiang University, Hangzhou City, Zhejiang Province, PR China

<sup>c</sup> Key Laboratory of Motor System Disease Research and Precision Therapy of Zhejiang Province, Hangzhou City, Zhejiang Province, PR China

<sup>d</sup> Clinical Research Center of Motor System Disease of Zhejiang Province, PR China

<sup>e</sup> State Key Laboratory of Fluid Power and Mechatronic Systems, College of Mechanical Engineering, Zhejiang University, Hangzhou, 310027, PR China

<sup>f</sup> Department of Orthopaedics, The First Affiliated Hospital, School of Medicine, Zhejiang University, Hangzhou, Zhejiang Province, PR China

## ARTICLE INFO

### Keywords:

Intervertebral disc degeneration  
Microneedle  
Exosomes  
Annulus fibrosus  
Mitophagy

## ABSTRACT

Low back pain is among the most grave public health concerns worldwide and the major clinical manifestation of intervertebral disc degeneration (IVDD). The destruction of annulus fibrosus (AF) is the primary cause of IVDD. A sustainable and stable treatment system for IVDD is lacking because of the special organizational structure and low nutrient supply of AF. We here found that IVDD results in the impaired mitochondrial function of AF tissue, and mitochondrial autophagy (mitophagy) plays a protective role in this process. We therefore reported a thread-structural microneedle (T-MN) matching the ring structure of AF. Based on the adsorption effect of laminin, our T-MN could load with bone marrow mesenchymal stem cell-derived exosomes to envelope the regulating mitophagy microRNA (miRNA 378), named as T-MN<sup>@EXO@miR-378</sup>. In general, we offered in situ locking in the defect site of AF to prevent nucleus pulposus leakage and promoted AF repair. The design of the thread structure was aimed at bionically matching the layered AF structure, thereby providing stronger adhesion. The T-MN<sup>@EXO@miR-378</sup> effectively attached to AF and slowly released therapeutic engineered exosomes, and prevented IVDD progression by restoring mitophagy, promoting AF cell proliferation and migration, and inhibiting the pathological remodeling of the extracellular matrix. This functional system can be used as an excellent tool for sustained drug release and has a certain prospect in substituting the conventional treatment of IVDD.

## 1. Introduction

Low back pain is a chronic problem associated with intervertebral disc (IVD) degeneration (IVDD) [1,2]. It is among the leading causes of disability worldwide and imposes a huge financial burden on patients and reduces their quality of life. For severe IVDD, the traditional

treatment method usually includes surgical resection, but this cannot restore the original disc function and increases the burden on adjacent discs [3]. The IVD consists of a cartilage endplate, an outer annulus fibrosus (AF), and an inner nucleus pulposus (NP) [4]. AF prevents the radial expansion of the NP disc by generating large circumferential stresses and resisting large tensile and compressive strains [5]. However,

Peer review under responsibility of KeAi Communications Co., Ltd.

\* Corresponding author. Department of Orthopedic Surgery, The Second Affiliated Hospital, Zhejiang University School of Medicine, Hangzhou City, Zhejiang Province, PR China.

\*\* Corresponding author.

\*\*\* Corresponding author. Department of Orthopedic Surgery, The Second Affiliated Hospital, Zhejiang University School of Medicine, Hangzhou City, Zhejiang Province, PR China.

E-mail addresses: [xu9709426@zju.edu.cn](mailto:xu9709426@zju.edu.cn) (J. Xu), [Yongqin@zju.edu.cn](mailto:Yongqin@zju.edu.cn) (Y. He), [zhangning@zju.edu.cn](mailto:zhangning@zju.edu.cn) (N. Zhang).

<sup>1</sup> The authors have contributed equally to this work and share first authorship.

<https://doi.org/10.1016/j.bioactmat.2024.03.006>

Received 29 November 2023; Received in revised form 9 February 2024; Accepted 4 March 2024

Available online 13 March 2024

2452-199X/© 2024 The Authors. Publishing services by Elsevier B.V. on behalf of KeAi Communications Co. Ltd. This is an open access article under the CC BY-NC-ND license (<http://creativecommons.org/licenses/by-nc-nd/4.0/>).

trauma or chronic strain may lead to tearing of the AF to varying degrees, eventually resulting in AF rupture. This rupture ultimately results in IVDD, including displacement, protrusion, or even prolapse of the NP without the protective shell, thereby reducing the water content, volume, and height of the IVD, and is the primary cause of IVDD [6]. AF rupture is due to the decrease in the extracellular matrix (ECM). The main underlying mechanism is the decrease in the ability to synthesize ECM and the increase in its decomposition ability [7]. AF is limited in its ability to heal itself, which results in residual granulation tissue, development of a chronic inflammatory state, and energy metabolism dysfunction [8,9]. This thus increases the risk of NP herniation, thereby making patients increasingly susceptible to IVDD. Mechanically, mitophagy disorder is a key player in IVD energy metabolism and ECM degradation, which is the etiology of AF rupture [9,10]. Therefore, mitophagy disorder must be addressed to restore energy metabolism and the steady state of ECM in AF.

Although some studies have proposed treatments for these problems [11,12], their results are not ideal. The reason is the difficulty in administering drugs because of disc degeneration. IVD is the largest avascular tissue in the whole body [13], and poor blood supply to this part leads to the unsatisfactory results of systemic administration of drugs. The IVD tissue is tough and does not support multiple administration. Moreover, a degenerative IVD has a complex microenvironment, with cellular stress in the implanted cell population because of elevated inflammatory cytokines and active proteases; decreased pH, glucose, and oxygen levels; and altered or unmanageable mechanical loads [14]. This environment also makes it difficult for the drug delivery system to release the drug continuously.

Bone marrow mesenchymal stem cell (BMSC)-derived exosomes promoting mitophagy only have a modest ability to restore the normal mitochondrial function and ECM homeostasis [15]. Numerous studies have shown that exosomes engineered with miRNA can effectively exhibit the physiological functions in treatment [16–19]. Exosomes can enclose miRNAs, and this biofilm structure protects miRNAs from degradation, thereby allowing easier endocytosis of miRNAs. MiR-378 is a miRNA that restores autophagy [20]. We therefore loaded miR-378 mimics into BMSC-derived exosomes, termed BMSC EXO@miR-378 [21]. BMSC EXO@miR-378 that have a certain effect on promoting the mitophagy recovery of IVDD is a reasonable choice for solving the IVDD problem. However, when injected directly, exosomes are not released and do not function in the IVD for long periods [22]. To overcome the limitations of traditional drug therapy, a new nanomedicine platform suitable for IVDD treatment must be developed to effectively overcome these problems.

To solve the aforementioned problems, we choose silk fibroin methacryloyl (SiIMA) with high hardness as the main raw material to reduce the risk of NP herniation. This material also has good biocompatibility. We specially designed and used 3D printing technology to prepare microneedles (T-MN) with a threaded structure to fit the IVD tissue. This structure can be locked into the IVD damaged tissue. This innovative design could improve in situ tissue fixation and stable administration of drug delivery systems for treatment. Additionally, laminin is beneficial for cell adhesion, migration, and differentiation and exerts an adsorption effect on exosomes [23]. The short arm of laminin mediates its polymerization and communicates with other ECM proteins. The end of the long arm controls transmitting interactions with cellular integrins of exosomes [24,25].

We here constructed a drug sustained release delivery system for the treatment of AF injury of IVDD with a spiral microneedle patch (T-MN@EXO@miR-378). Specifically, we prepared a thread-structural microneedle loaded with EXO@miR-378 based on the SiIMA composite laminin. SiIMA has sufficient hardness that allows the microneedle patch adhere closely to the damaged AF, and laminins can adsorb and slowly release exosomes. Our results presented the unique characteristics of T-MN@EXO@miR-378 as a treatment system in repairing damaged AF. Furthermore, the impaired mitophagy of AF cells lead to ECM

destruction and thus severe IVDD. Therefore, we loaded EXO@miR-378 into T-MN to restore the damaged mitophagy function of AF and the ECM steady state. Overall, our data provided insights for a long-term therapeutic strategy based on the recovery of AF-damaged mitophagy, which offers a new possibility for the clinical treatment of IVDD (see Scheme 1).

## 2. Results

### 2.1. Mitophagy of annulus fibrosus plays a protectional role in IVDD

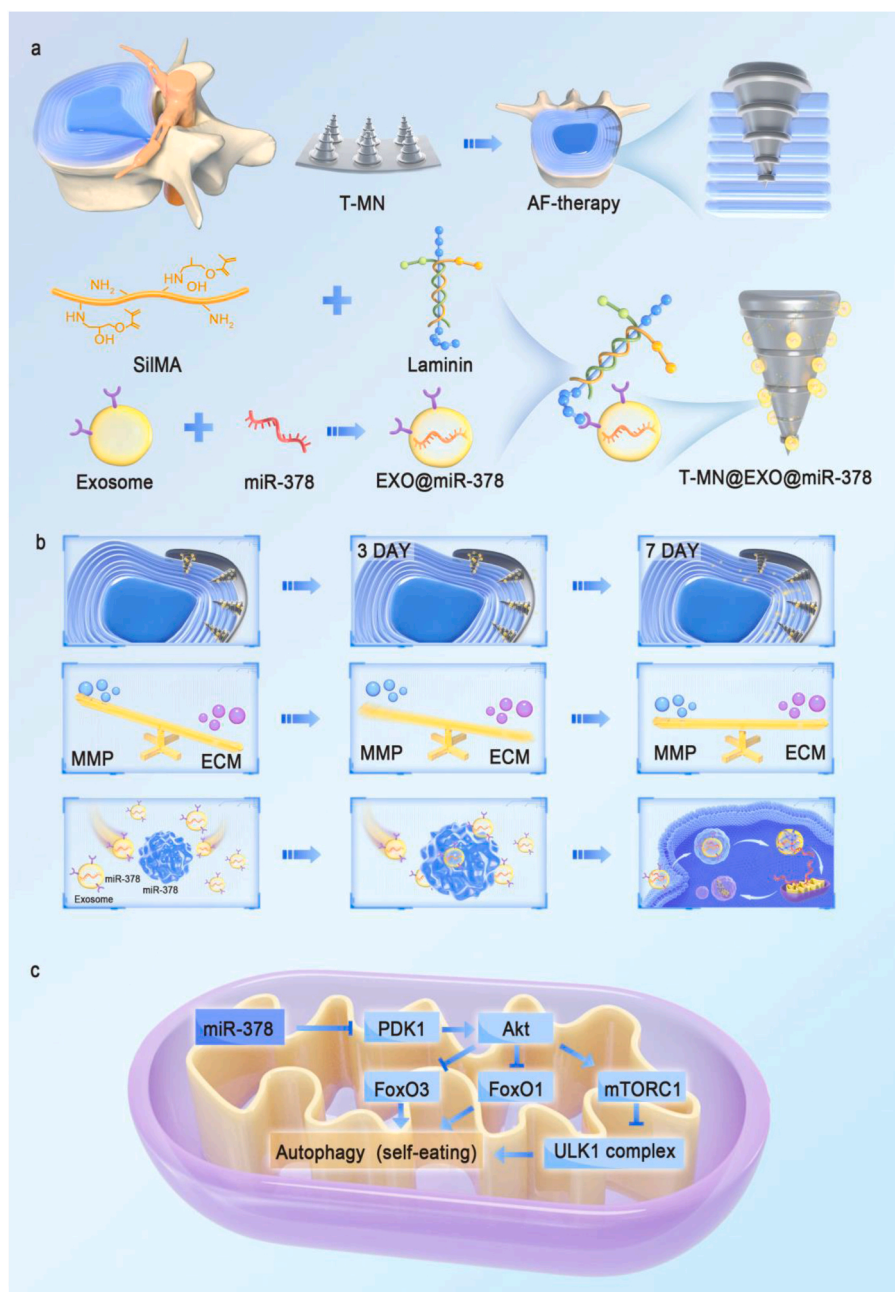
The destruction of AF plays a crucial role in IVDD (Fig. 1A). To study the genes responsible for human AF degeneration, we analyzed the single-cell RNA-seq dataset GSE199866 in GEO [26] as well as differentially expressed genes (DEGs) between the degenerated and normal AF cells from humans (Fig. 1B, Figs. S1–3). KEGG analysis revealed the presence of DEGs in autophagy (SQSTM1/BNIP3/WDR45B/CTSL/UBC/CTSD) and mitophagy (SQS27TM1/BNIP3/UBC/ATF4) (Fig. 1C). Therefore, we speculated that autophagy and mitophagy play crucial roles in IVD protection.

We then induced the rat AF cell degeneration model with IL-1 $\beta$  as the experimental group and used the untreated rat AF cell model as the control group. RNA-seq analysis of three control groups and three experimental groups revealed seven autophagy-related DEGs, namely Foxo1, Tsc1, Ern1, Dlc1, Wdfy3, Fos, and Map1lc3a (Fig. 1D–F). Through KEGG analysis (Fig. 1G) and analysis of GO annotations (Fig. 1H), we found that these autophagy-related genes regulate cellular processes and biological regulatory functions, and are also closely related to cell membrane components. Tsc1 was enriched in the PI3K-Akt signaling pathway; Ern1 and Fos were enriched in the apoptosis signaling pathway; Map1lc3a, Foxo1, Ern1, Fos, and Tsc1 were closely related to a response to the stimulus; and Dlc1, Ern1, and Wdfy3 were closely related to the membrane part (Fig. 1H). This proved that the degenerated AF damaged the mitochondrial membrane because of autophagy injury. Next, the mitophagy level in the degenerated AF cells was determined through the protein expression level. Western blotting revealed that the mitophagy level of the degenerated AF cells significantly decreased, the expression of the mitophagy-inhibiting protein PINK1 increased by 35%, and the expression of the mitophagy-promoting proteins Parkin and LC3II/I decreased by 25% and 20%, respectively. Fundc1 is a gene encoding proteins related to selective autophagy and mitophagy [27]. A 49% decrease was observed in the levels of Fundc1 protein expression in the experimental group (Fig. 1I and J). This demonstrated that mitophagy of AF cells was impaired in the AF degenerative model.

To study the effect of autophagy on IVDD, we specially constructed Fundc1 (mitophagy associated gene) Knockout (KO) mice and verified its role through a tail-puncture disease model (Fig. 1K). Hematoxylin-eosin (HE) staining revealed no significant difference in morphology between the wild-type (WT) group and the Fundc1-KO group without injury. The AF structure was intact in all groups. Compared with the WT injured group, the Fundc1-KO injured group exhibited more obvious disc structure injury and a higher decrease in disc height (Fig. 1L). Safranin O-fast green (SO) staining revealed no significant difference in cartilage components between the WT and Fundc1-KO groups. However, compared with the WT injured group, the decrease in the AF cartilage components of the Fundc1-KO injured group was more significant (Fig. 1M). These results proved that mitophagy plays a crucial protective role in the degenerated AF cells. Therefore, restoring mitophagy in degenerated AF is a promising treatment for IVDD.

### 2.2. Preparation and characterization of AF-matching microneedles, T-MN@EXO@miR-378

We demonstrated the critical influence of mitophagy of AF cells in



**Scheme 1.** Annulus fibrosus tissue-matching thread-structural microneedles loaded with engineered exosomes for annulus fibrosus repair by regulating mitophagy recovery and extracellular matrix homeostasis. (a) Preparation of T-MN@EXO@miR-378 and engineered exosomes. (b) T-MN@EXO@miR-378 sustainably release exosomes and regulate ECM and mitophagy. (c) The regulatory pathway of miR-378 on mitophagy.

IVDD. However, improvement in mitophagy of the AF cells is associated with many challenges because of its tough tissue properties and lack of nutrient supply. To bring drugs into deeper AF tissues, we designed the MN structure and used 3D printing to create a mold for the MNs. SiMA was selected as the main raw material for MNs to attach closely to the rigid structure of the AF (Fig. 2A). The smooth structure is easy to slide or move out of place, so we designed a MN with a threaded structure, similar to the tapered thread. This structure can increase the friction to ensure that the T-MN patch is more firmly fixed on the tissue to prevent leakage of the flowing NP as well as make the threaded structure increase the contact area with the AF to increase the drug release area (Fig. 2B). The threaded structure can be changed by adjusting the light curing time and height of each layer. Finally, the T-MN patch was designed as an array of  $23 \times 23$  MNs with a height of  $500 \mu\text{m}$  and a

bottom diameter of  $200 \mu\text{m}$ . The MNs have a large height-to-diameter ratio so that the sharp tips can easily penetrate the AF.

The repair of IVDD is a long-term process. To increase the ability of T-MN to sustainably release exosomes, laminin was introduced into our system to adsorb exosomes. This was because the long-arm ends of laminin can interact with integrins and growth factors on exosomes (Fig. 2C). Because of laminin adsorption and the porous structure inside the hydrogel, the exosomes penetrated into the interior of the T-MN and adhered to its surface (Fig. 2D). Fourier-transform infrared spectroscopy confirmed the successful mixing of laminin and SiMA. Both SiMA and laminin are proteins with typical characteristic absorption peaks of amide I band ( $\text{C}=\text{O}$  stretching vibration at  $1700\text{--}1600 \text{ cm}^{-1}$ ), amide II band ( $\text{N-H}$  stretching and bending vibration at  $1600\text{--}1500 \text{ cm}^{-1}$ ), and amide III band ( $\text{C-N}$  stretching vibration at  $1330\text{--}1220 \text{ cm}^{-1}$ ) and the

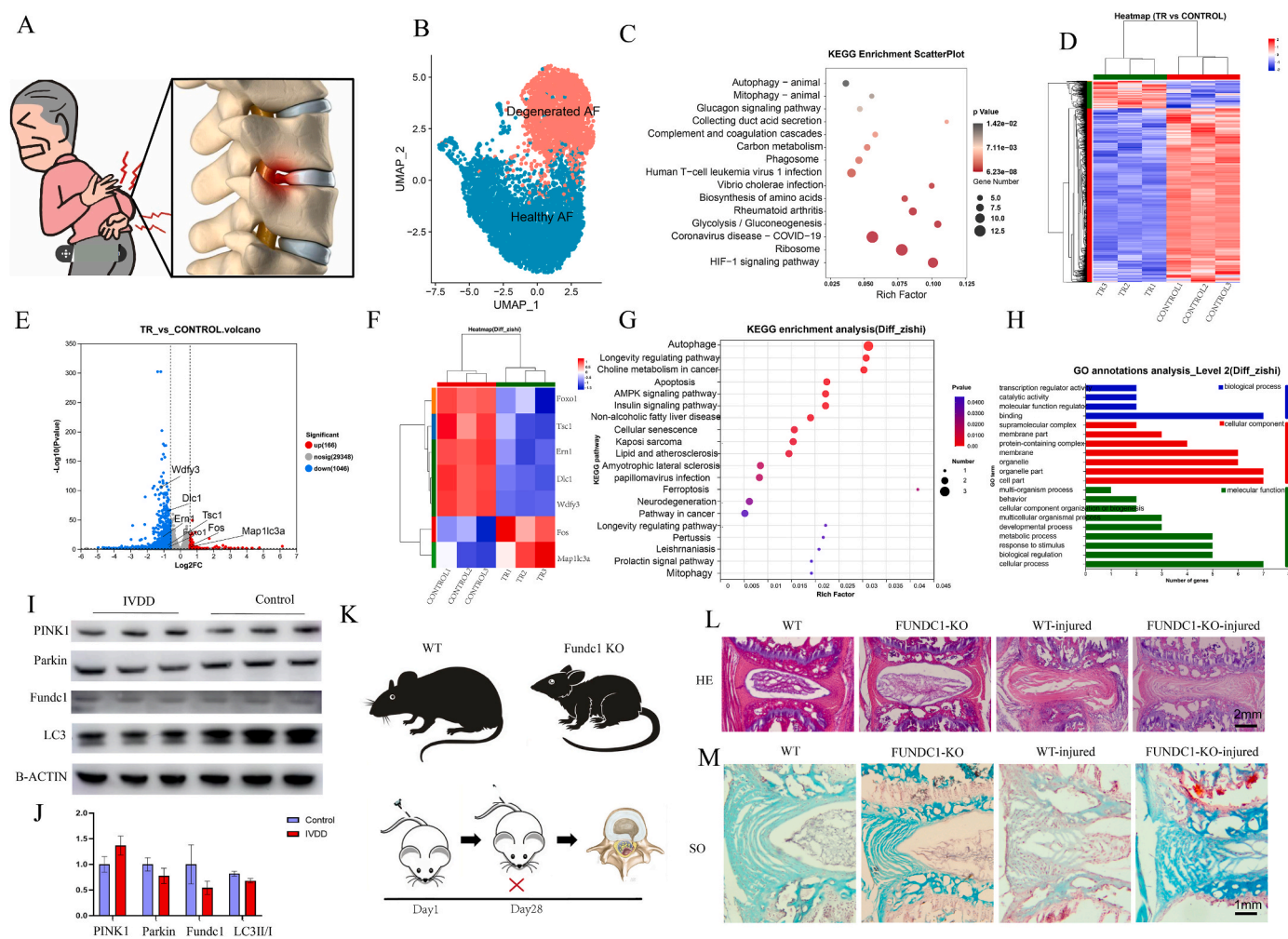


**Fig. 1.** Mitophagy-related gene is highly changed in the degenerated annulus fibrosus cells and plays a protective role in IVDD. (A) Schematic illustration of IVDD. (B) Umap of the dataset from human IVD. (C) KEGG enrichment analysis of the DEGs between degenerated AF cells and normal AF cells from human IVD. (D) Heat map of mRNA transcriptional profiling between the control and experimental groups from rat IVD *in vitro*. (E) Volcano plot of DEGs between the experimental and control groups. (F) Heat map of the mRNA transcriptional profiling between the control and experimental groups depicting the DEGs involved in autophagy. (G) KEGG enrichment analysis of the DEGs involved in autophagy. (H) GO annotations plot of mRNA transcriptional profiling between the control and experimental groups depicting the DEGs involved in autophagy. (I) Protein expressions of the characteristic proteins of mitophagy of experimental and control groups. (J) Quantification of the protein expression.  $\beta$ -actin served as the loading control. Data are presented as the mean  $\pm$  SD ( $n = 3$ ); \* $p < 0.05$ , \*\* $p < 0.01$  VS the control group. (K) Schematic illustration of Fundc1 KO mice, IVDD model, and sampling process. (L) Images of HE and safranin O (M) staining from each group.

characteristic absorption peak of the amide group (N–H stretching vibration at  $3500\text{--}3100\text{ cm}^{-1}$ ). Laminin is formed by combining an  $\alpha$  chain and two  $\beta$  chains through a disulfide bond, and its characteristic absorption peak is observed at  $555\text{ cm}^{-1}$ . The amide I, II, and III peaks of SilMA respectively appeared at  $1637$ ,  $1515$ , and  $1237\text{ cm}^{-1}$ , which are fully consistent with the  $\beta$ -folded conformation. After SilMA was mixed with laminin, the amide band of SilMA gradually transformed to a  $\alpha$ -helical conformation, indicating that laminin was successfully compounded. Laminin led to the blue shift of all SilMA peaks and increased peak intensity, thereby allowing the substance to be more active for exosome adsorption.

Swelling properties can reflect the hydrogel's capacity to carry drugs/growth factors and the rate of material exchange with the external environment. As illustrated in Fig. 2D–F, 25% SilMA exhibited the lowest swelling ratio, which is mainly because of the high degree of crosslinking at a high concentration and the formation of relatively small pores. The concentration with the highest porosity should be selected to ensure the release of drug/factors. On the other hand, if the swelling is too large, T-MN easily displaces or protrudes, leading to local inflammation [28]. Moreover, as the porosity of the gel decreases, its

overall strength increases, possibly causing further compression damage to the spinal cord tissue. Therefore, the swelling properties should not be too high.

When subjected to external forces, NP evenly transfers the pressure to all parts of the AF, allowing it to lengthen to absorb the forces. Therefore, the material for AF repair should have adequate mechanical strength [29]. We tested the tensile and compressive moduli of four hydrogel concentrations. Both tensile and compressive moduli tended to increase with incremental concentrations of SilMA (Fig. 2G and H). Of note, a remarkable growth was noted between the 15% and 20% concentrations, possibly because of the different degrees of crosslinking under the equal duration of UV light irradiation. We conjecture that this is because the transition from incomplete crosslinking to complete crosslinking occurs between the aforementioned concentrations. Considering the swelling and mechanical performance, 20% SilMA was selected as the major component.

MNs have no more crucial function than adhering to the tissue to deliver drugs/factors [30]. Hence, the tip strength of T-MN is of particular concern. The fracture force of every single needle was examined (Figs. 2I), and 20% SilMA T-MNs could withstand a force

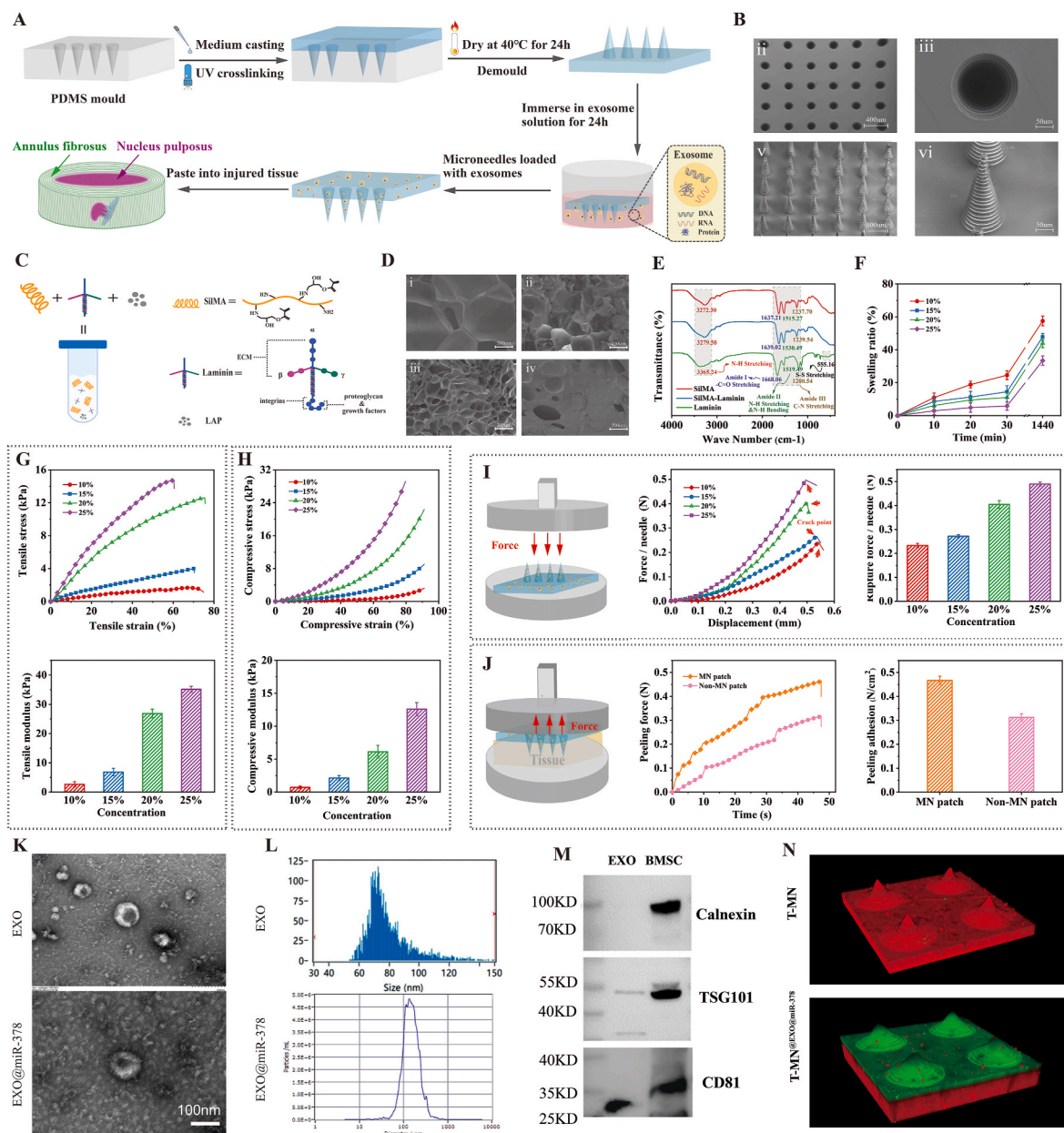


**Fig. 2.** Preparation and characterization of T-MN<sup>@</sup>EXO@miR-378. (A) Procedure of the fabrication of T-MN<sup>@</sup>EXO@miR-378. (B) (i) SEM image of microholes in PDMS mold. Scale bar: 400  $\mu$ m. (ii) SEM image of a single microhole. Scale bar: 50  $\mu$ m. (iii) SEM image of T-MN<sup>@</sup>EXO@miR-378. Scale bar: 400  $\mu$ m. (iv) SEM image of a single T-MN<sup>@</sup>EXO@miR-378. Scale bar: 50  $\mu$ m. (C) Preparation of the SilMA-laminin hydrogel solution. (D) SEM images of microscopically porous of SilMA hydrogel at different concentrations: (i) 10%, (ii) 15%, (iii) 20%, (iv) 25%. Scale bars: 200  $\mu$ m. (E) The FTIR spectra of SilMA, laminin, and SilMA-laminin. (F) The swelling ratio of SilMA hydrogel at different concentrations over time. (G) Tensile stress-strain curve and modulus of SilMA hydrogel at different concentrations. (H) Compressive stress-strain curve and modulus of SilMA hydrogel at different concentrations. (I) Force-displacement curve and rupture force of a single microneedle of SilMA hydrogel at different concentrations. (J) Peeling force and peeling adhesion of the patch with the T-MN structure and the patch without the MN structure. (K) TEM analysis of exosome (EXO) and EXO@miR-378. Scale bar = 0.2  $\mu$ m. (L) NTA analysis of exosome and EXO@miR-378. (M) Exosome characterization of calnexin, TSG101, and CD81 by Western blotting. (N) Fluorescence images of T-MN and T-MN<sup>@</sup>EXO@miR-378 (Red: T-MN; Green: exosomes).

>0.4 N, which is sufficient for inserting the superficial layer of the AF. Additionally, to verify that the T-MN patch has a better adhesion effect than the patch without microstructures, the peeling experiment was conducted (Fig. 2J). The maximum peeling adhesion of the T-MN patch was 0.47 N, which was 1.6 times that of the patch without microstructures. This strongly demonstrates the necessity for MN structures. The rheological performance of T-MN hydrogels were evaluated. Photo-rheology experiments demonstrated that all concentrations of SilMA T-MN hydrogels could undergo photocrosslinking and solidify within 20 s. Prior to crosslinking, T-MN existed in a liquid state, exhibiting a loss modulus greater than the storage modulus, indicating viscous

deformation. Upon crosslinking, T-MN transformed into a gel state, with the storage modulus exceeding the loss modulus, signifying elastic deformation. As the concentration of SilMA T-MN increased, the storage modulus of the solidified hydrogel gradually rose. This trend aligns with the behavior observed in compression and tensile modulus (Fig. S10).

Subsequently, we verified the characterization of exosomes and EXO@miR-378. MiR-378 were loaded in exosomes by using ultrasonic shock. The ultrasonic shock method caused slight shape changes in the exosome membrane (Fig. 2K). The exosome size was also within the normal range of approximately 100 nm (Fig. 2L). The surface proteins CD81 and TSG101 were also positive, whereas the negative protein

calnexin was not expressed, thereby proving the purity of the proposed exosomes (Fig. 2M). Next, we tested the loading efficiency and exosome-release property of T-MN, and the results showed that T-MN can load about 1 mg exosomes and about 80% of exosomes was released in three days (Fig. S9, Fig. S14). After EXO@miR-378 was co-stained with the DID dye solution for 1 h, the exosomes were incubated with the tip part of T-MN for 24 h. Scanning using a confocal microscope revealed that EXO@miR-378 was adsorbed on the surface of T-MN (Fig. 2N). In conclusion, we constructed T-MN@EXO@miR-378 that can adapt to the AF structure and carry EXO@miR-378.

### 2.3. T-MN@EXO@miR-378 mediate ECM metabolism and AF cells migration

Firstly, we verified the effect of miR-378 on the autophagy pathway. Overexpression of miR-378 by transfection of specific mimics into AF cells for miR-378 increased the lipidation of LC3, whereas inhibition of miR-378 by transfection of specific antagonist for miR-378 (Ant-378) decreased the lipidation of LC3 in AF cells (Figs. S11 and S12). We then conducted a preliminary verification of the *in vivo* therapeutic effect of T-MN@EXO@miR-378 on AF cells. T-MN@EXO@miR-378 was inverted in the medium so as to release EXO@miR-378 into the medium, which was then absorbed by the AF cells (Fig. 3A).

To detect the protective effect of T-MN@EXO@miR-378 on degenerated

AF cells, the AF cells were pretreated with T-MN, T-MN loaded with the normal BMSC exosome (T-MN@EXO), and T-MN@EXO@miR-378 and co-cultured with IL-1 $\beta$  for 24 h. The T-MN@EXO group exhibited the reduced metalloproteinase capacity of the AF cells. T-MN@EXO reduced the expression of MMP13 by 42%, whereas T-MN@EXO@miR-378 reduced it by 49% (Fig. 3B). This implies that T-MN@EXO and T-MN@EXO@miR-378 both can inhibit degenerated AF cells to degrade the ECM. T-MN@EXO and T-MN@EXO@miR-378 increased Col I protein expression by 72% and 150%, respectively (Fig. 3C). This proved that T-MN@EXO@miR-378 has a better ability to promote ECM synthesis by the degraded AF cells than T-MN@EXO. The same results were also obtained using immunofluorescence methods (Fig. 3D and E). Thus, we proved that T-MN@EXO@miR-378 had a significantly higher ability to restore ECM in a degenerative environment.

Next, to verify the effect of T-MN@EXO@miR-378 on AF cell migration, we traced a straight line along the bottom of the Petri dish to simulate the AF cell defect when the AF is injured. The crawling distance of the AF cells was observed after 12 and 24 h, respectively. The T-MN@EXO and T-MN@EXO@miR-378 groups migrated nearly three times more (35% more migration) than the IL-1 $\beta$  group at 12 and 24 h (Fig. 3F–H). No significant difference in migration was observed between the T-MN@EXO and T-MN@EXO@miR-378 groups. Thus, T-MN@EXO@miR-378 has the ability to treat IVDD by increasing the number of normal AF cells and the gross amount of ECM at the damaged site, which is a prerequisite for repairing

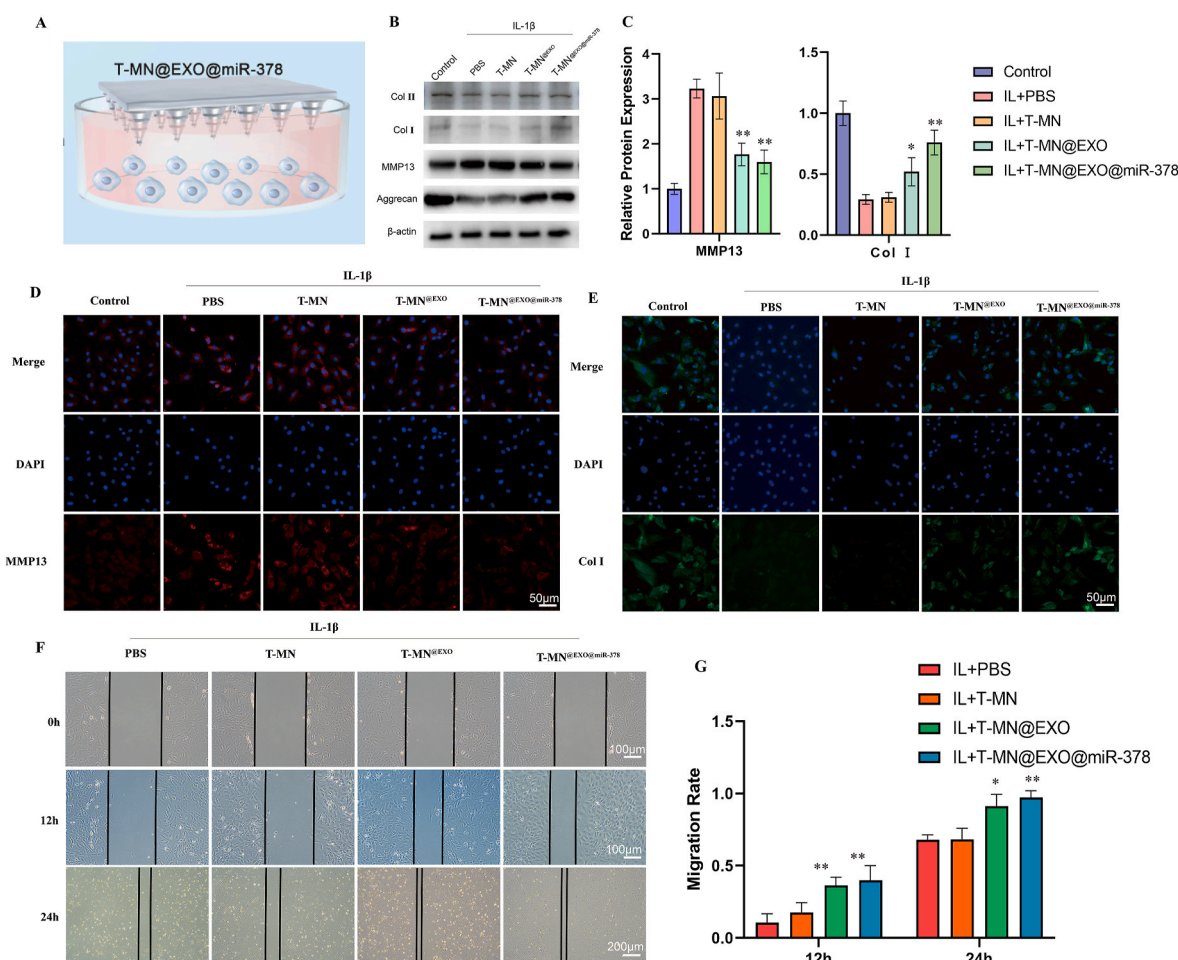


**Fig. 3.** T-MN@EXO@miR-378 promotes ECM synthesis, inhibits ECM decomposition, and promotes AF cells' migration. (A) Schematic illustration of the effect of T-MN@EXO@miR-378 on AF cells. (B) Protein expressions of Col I, Col II, aggrecan, and MMP13 of control, IL-1 $\beta$ , T-MN, T-MN@EXO, and T-MN@EXO@miR-378 groups. (C) Quantification of Col I and MMP13 protein expression.  $\beta$ -actin served as the loading control. Data are presented as the mean  $\pm$  SD ( $n = 3$ ). \* $p < 0.05$ , \*\* $p < 0.01$  VS the control group. (D) Fluorescence images of MMP13 from each group. (E) Fluorescence images of Col I after IL-1 $\beta$  stimulation in each group. (F) A migration experiment of each group. (G) Quantitative analysis of the migration experiment of the migration rate in each group for 12 h and 24 h, data are presented as the mean  $\pm$  SD ( $n = 3$ ). \* $p < 0.05$ , \*\* $p < 0.01$  VS the IL + PBS group.

the damaged AF.

#### 2.4. T-MN<sup>@EXO@miR-378</sup> promote mitophagy of AF cells

Based on the results of previous RNA-seq analyses, we demonstrated that mitophagy plays a key role in IVDD. High levels of reactive oxygen species (ROS) can cause mitochondrial respiratory bursts, leading to mitochondrial damage [31]. To verify that T-MN<sup>@EXO@miR-378</sup> restores normal mitochondrial function, ROS levels in each group were first measured (Fig. S4). T-MN<sup>@EXO@miR-378</sup> reduced 35% ROS in the degenerated AF cells. To determine the effect of T-MN<sup>@EXO@miR-378</sup> on the mitochondrial depolarization function, the JC-1 kit was used to detect the depolarization of the mitochondria membrane potential, which directly reflects the respiratory function and energy generation level of mitochondria. T-MN<sup>@EXO</sup> increased the level of JC-1 aggregates/monomers in the degraded AF cells by 275%, while the value for T-MN<sup>@EXO@miR-378</sup> was better, which could recover up to 92% of the control group value (Fig. 4A, Fig. S5). Similar results were also observed for mitochondrial morphology. Obvious cavitation of mitochondrial cristae was noted in the degenerated AF cells, which could be partially restored to the normal shape after treatment with T-MN<sup>@EXO@miR-378</sup> (Fig. 4C). These results demonstrated that T-MN<sup>@EXO@miR-378</sup> restores

mitochondrial morphology and function to treat degenerative AF.

To verify whether T-MN<sup>@EXO@miR-378</sup> mediates mitochondrial quality by restoring the mitophagy pathway, the characterized mitophagy protein expression level was determined through western blotting. T-MN<sup>@EXO@miR-378</sup> decreased the expression of the mitophagy-inhibiting protein p62 and PINK1 by 64% and 60%, respectively, whereas increased the expression of the mitophagy-promoting protein Fundc1 by 48% (Fig. 4B, Fig. S6). Immunofluorescence staining was performed on mitophagy markers and demonstrated similar results. T-MN<sup>@EXO</sup> and T-MN<sup>@EXO@miR-378</sup> decreased the p62 protein expression level by 28% and 71%, respectively (Fig. 4D, Fig. S7). T-MN<sup>@EXO</sup> and T-MN<sup>@EXO@miR-378</sup> increased the LC3 protein expression level of the degenerated AF cells by 19% and 175%, respectively (Fig. 4E, Fig. S8). This proved that T-MN<sup>@EXO@miR-378</sup> controlled the normal morphology and function of mitochondria by restoring the mitophagy level.

Subsequently, we completely verified the effect of miR-378 on the autophagy pathway. T-MN<sup>@EXO@miR-378</sup> significantly affected autophagy activation through the PDK1-Akt pathway (Fig. 4F). Western blotting revealed that T-MN<sup>@EXO@miR-378</sup> reduced the PDK protein expression level and the pAkt protein expression level. T-MN<sup>@EXO@miR-378</sup> promoted the protein expression level of FoxO1 and FoxO3 in the downstream of the PDK1-Akt pathway (Fig. 4G). These

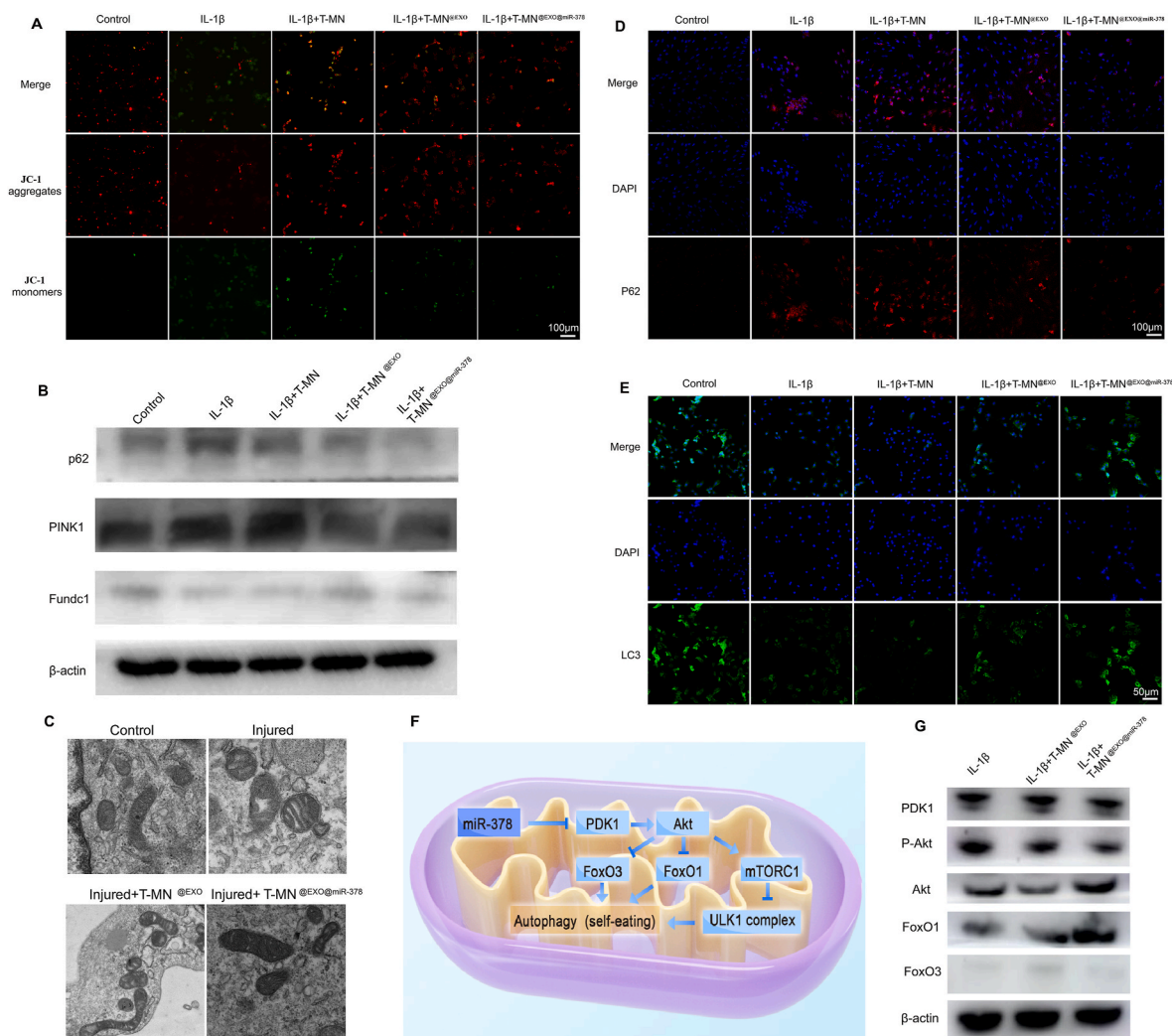


**Fig. 4.** T-MN<sup>@EXO@miR-378</sup> promote mitophagy and mitochondrial function in AF cells. (A) JC-1 Fluorogram of the control, IL-1 $\beta$ , T-MN, T-MN<sup>@EXO</sup>, and T-MN<sup>@EXO@miR-378</sup> groups. (B) Protein expressions of p62, PINK1, and Fundc1 of each group. (C) TEM of mitochondria of each group. (D) Fluorescence images of P62 after IL-1 $\beta$  stimulation from each group. (E) Fluorescence images of LC3 after IL-1 $\beta$  stimulation of each group. (F) Schematic illustration of the pathway of miR-378 restoration autophagy. (G) Protein expressions of PDK1, P-Akt, Akt, FoxO1, and FoxO3 of each group. Data are presented as the mean  $\pm$  SD (n = 3). \*p < 0.05, \*\*p < 0.01 VS the control group.

results demonstrated that EXO@miR-378 plays a key role in promoting AF mitophagy through T-MN@EXO@miR-378.

## 2.5. T-MN@EXO@miR-378 keeps releasing EXO@miR-378 to promote AF repair in vivo

To further demonstrate the IVD-protecting ability of T-MN@EXO@miR-378, we established a model of AF injury in the caudal vertebral segment of rats and tested the effect of T-MN@EXO@miR-378 *in vivo*. After AF injury, T-MN, T-MN@EXO, and T-MN@EXO@miR-378 was applied to the injury site of the rats according to the respective groups they belonged. Then, musculocutaneous suture was performed (Fig. 5A and B). The height of damaged discs decreases over time. At 4 weeks, the T-MN@EXO@miR-378 group retained 28% more-disc height index (DHI%) than the injured group. At 8 weeks, the T-MN@EXO@miR-378 group

retained 31% more DHI than the injured group (Fig. 5C–E). Next, we conducted MRI to test water content of nucleus pulposus, which demonstrated that T-MN@EXO@miR-378 effectively promote the hydration state of nucleus pulposus (Fig. S17). The cross-sectional morphology of the IVD was observed after 8 weeks of treatment. The T-MN@EXO group exhibited a relatively better morphology (Fig. 5F). These observations proved that T-MN@EXO@miR-378 maintains the disc height and morphology after AF injury.

Subsequently, the sustained release effect of T-MN@EXO@miR-378 was verified *in vivo*. After the exosomes were stained with DID, the effects of T-MN with and without laminin were examined. Laminin-free T-MN was used as a control. T-MN with laminin maintained 85% exosome content after 1 week. However, T-MN without laminin maintained 51% exosome content for the same duration. The total amount and duration of exosome adsorption of laminin-containing T-MN was higher than those of

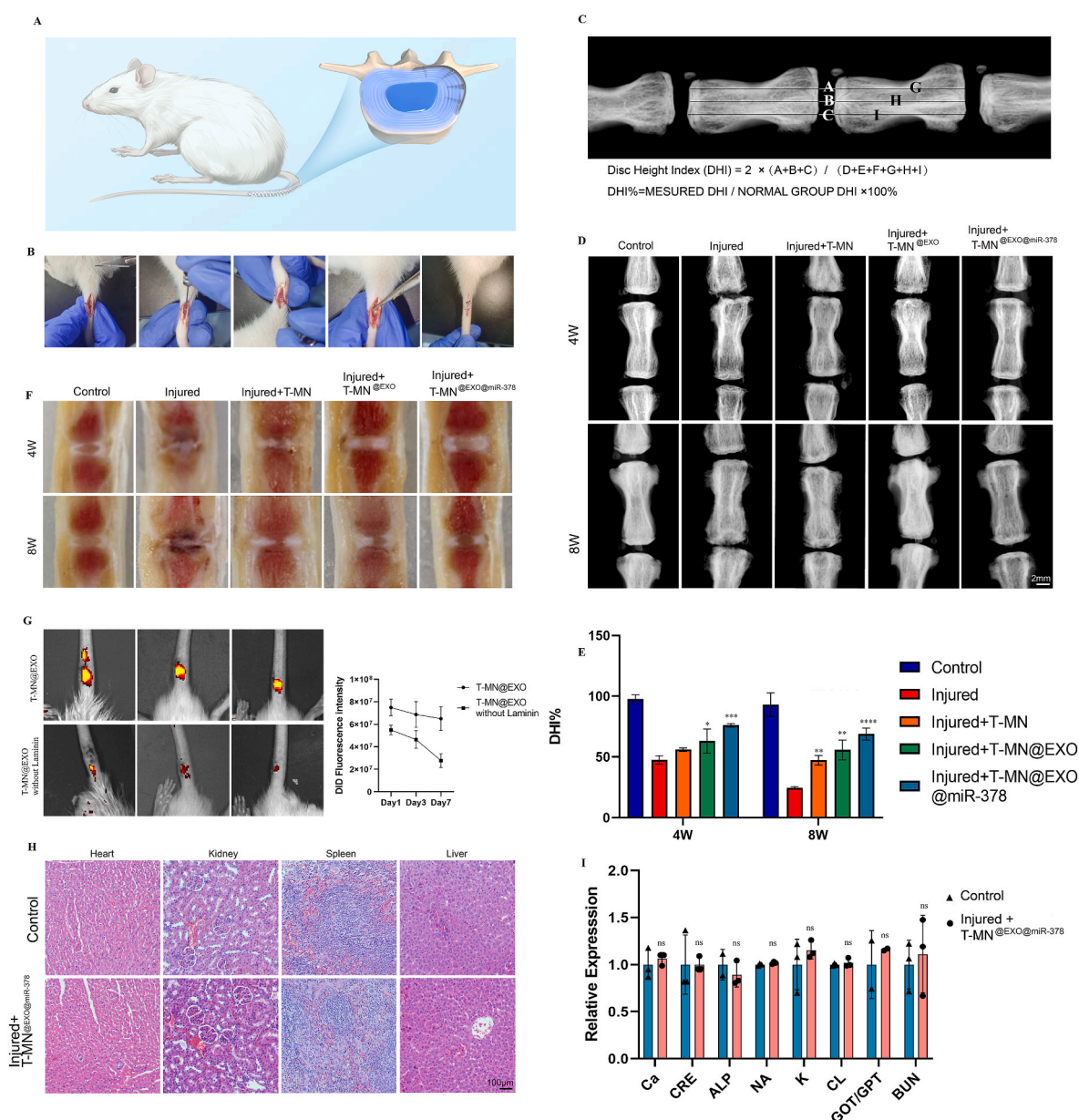


**Fig. 5.** T-MN@EXO@miR-378 release exosomes sustainably to save the disc height *in vivo*. (A) Schematic illustration of T-MN@EXO@miR-378 in rat IVD repair. (B) Schematic illustration of surgery for AF injury. (C) The calculation method of the disc height index. (D) X-ray images of the intervertebral disc at 4 and 8 weeks from each group. (E) DHI was evaluated at 4 and 8 weeks. Data are presented as the mean  $\pm$  SD; \* $P < 0.05$ . (F) Visual view of the disc from each group. (G) DID fluorescence intensity of exosome *in vivo* at 1, 3, and 7 days. (H) HE images of the heart, kidney, spleen, and liver from the control and T-MN@EXO@miR-378 groups. (I) The relative expression of blood biochemical indices, including Ca, CRE, ALP, Na, K, Cl, GOT/GPT, BUN, based on the control group.

laminin-free T-MN. After 1 week, the exosome content in the laminin-containing laminin group was 130% more than that in the laminin-free T-MN group (Fig. 5G). These results explained why T-MN<sup>@EXO@miR-378</sup> continues to exert a good therapeutic effect after 8 weeks.

To verify whether the use of T-MN<sup>@EXO@miR-378</sup> has an impact on other organs. The organs of the treated rats were stained with HE, and blood biochemical markers were measured. Organs from the treated mice were stained with HE for histopathological evaluation. The results indicated that the local ultralong retention of T-MN<sup>@EXO@miR-378</sup> caused no inflammatory response in the heart, liver, spleen, and kidney (Fig. 5H). Similarly, the use of T-MN<sup>@EXO@miR-378</sup> had a neglective effect on the blood biochemistry of the heart, liver, and kidney, including Ca, CRE, ALP, Na, K, Cl, GOT/GPT, and BUN (Fig. 5I). T-MN<sup>@EXO@miR-378</sup> thus had a protective effect on IVD without affecting other organs *in vivo*, which indicates its great clinical application potential.

## 2.6. T-MN<sup>@EXO@miR-378</sup> recover ECM environment homeostasis and mitophagy of AF *in vivo*

To better understand the influence of T-MN<sup>@EXO@miR-378</sup> on AF

organization, we performed staining with HE and SO in each group. Histologically, SO staining revealed that T-MN<sup>@EXO@miR-378</sup> could better protect the cartilage components (red area) of the inner AF and NP (Fig. 6A). In each group, HE staining exhibited changes in the disc status after the treatment of AF injury (Fig. 6B). At the same time, the T-MN group exhibited a general treatment effect, while the T-MN<sup>@EXO</sup> and T-MN<sup>@EXO@miR-378</sup> groups received better protection for the overall disc morphology. Ocal observation unveiled that the T-MN<sup>@EXO@miR-378</sup> group had better continuity of the layered structure at the injured site, and this was also observed at week 8. This proves the structural protection effect of T-MN<sup>@EXO@miR-378</sup> on the damaged AF.

To further verify that T-MN<sup>@EXO@miR-378</sup> treats IVDD by restoring mitophagy and regulating ECM stability *in vivo*, IHC staining was performed. The IHC analysis confirmed that the expression of the mitophagy-promoting proteins (Fundc1, Parkin) was low in the injured group, whereas that of the mitophagy-inhibiting protein (PINK1) was high in the injured group. T-MN<sup>@EXO@miR-378</sup> promotes the expression of the mitophagy-promoting proteins and inhibits the expression of the mitophagy-inhibiting protein, which also enables it to regulate ECM homeostasis (Fig. 6C and D, S13A, S13B). To further verify the role of mitophagy in IVDD, we established an IVD acupuncture model in Fundc1 KO mice. The AF-impaired Fundc1 KO mice could be more

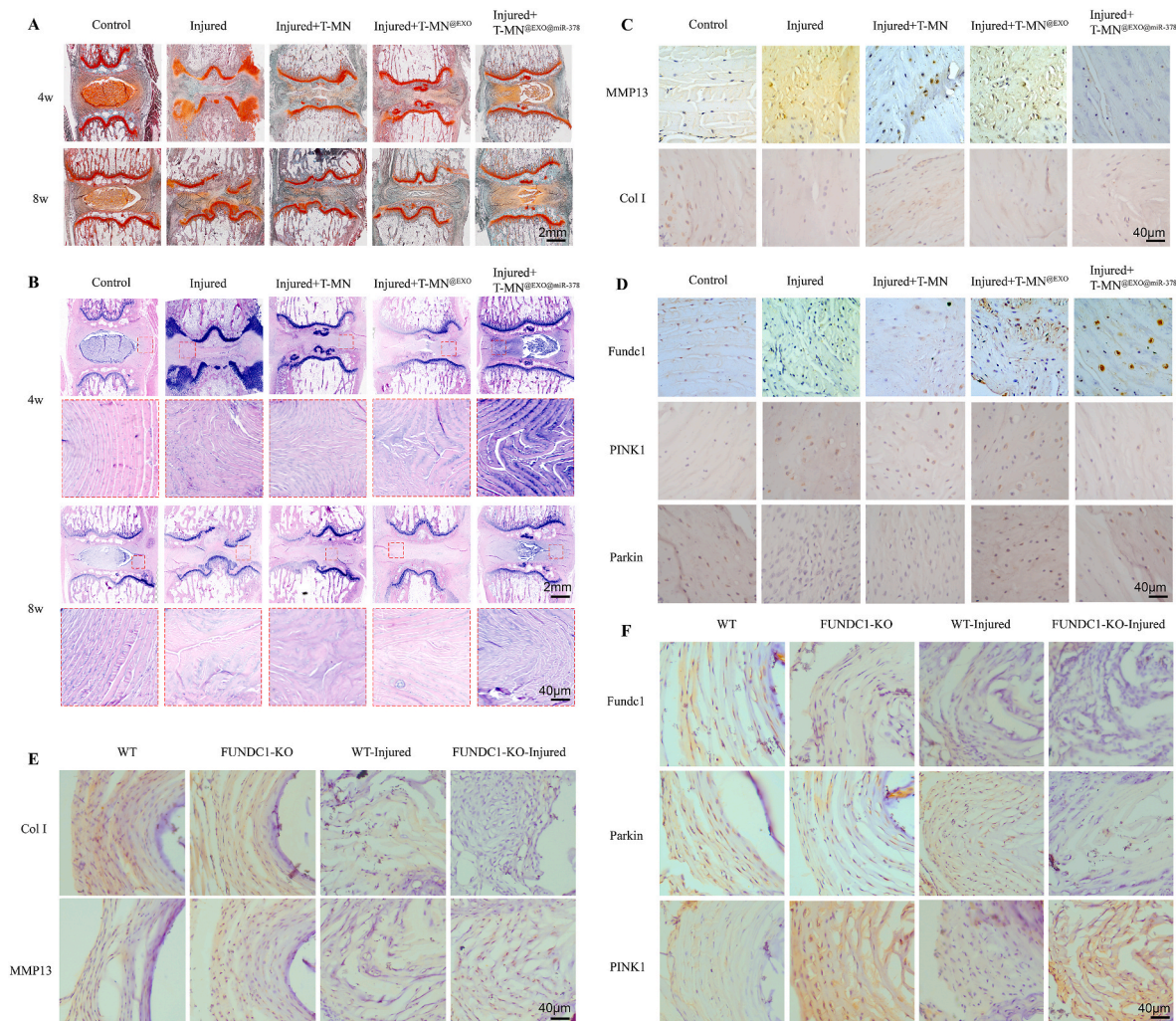


**Fig. 6.** T-MN<sup>@EXO@miR-378</sup> promotes ECM synthesis, inhibits ECM decomposition, and promotes mitophagy *in vivo*. (A) Images of safranin O from control, injured, T-MN, T-MN<sup>@EXO</sup>, and T-MN<sup>@EXO@miR-378</sup> groups. Scale bar = 1 mm. (B) Images of HE staining from each group. (C) Immunohistochemical detection of MMP13 and Col I. (D) Immunohistochemical detection of fundc1, pink1, and parkin of each group. (E) Immunohistochemical detection of MMP13 and Col I from WT, FUNDC1-KO, WT-Injured, and FUNDC1-KO-Injured groups. (F) Immunohistochemical detection fundc1, pink1, and parkin from WT, FUNDC1-KO, WT-Injured, and FUNDC1-KO-Injured groups.

severely impaired in mitophagy and had more severe ECM damage (Fig. 6E and F, S13C, S13D). These results proved the harmful effect of impaired mitophagy on AF and that T-MN<sup>@EXO@miR-378</sup> restores mitophagy in a targeted manner to offer protection to AF.

### 3. Discussion

The results of the current available treatment methods for IVD, including physical therapy, pharmacotherapy, and surgical intervention, are not satisfactory [32]. These methods only provide symptomatic relief and do not slow down or prevent the underlying biological processes, thereby allowing further tissue damage. Increasing evidence has recently suggested that disrupted mitophagy contributes to IVDD development [9,16]. The primary therapeutic targets for progressive IVDD are associated with the deactivation of matrix-degrading enzymes and limited matrix regeneration capacity, both of which are closely related to mitophagy dysfunction. Restoring mitophagy effectively halts IVDD progression by restoring cellular energy homeostasis and ECM stability. In some studies, IVDD was treated by injecting MSCs [33]. However, injecting stem cells with a normal mitochondrial function directly into the body so that they differentiate into AF cells is challenging because of the inflammatory microenvironment within the IVD and ethical issues [13,34]. By contrast, the engineered exosome therapy has been demonstrated to enhance ECM repair capability and mitophagy levels in the IVD and has been found to be beneficial for IVDD treatment [35]. We here report an engineered exosomes sustained release delivery system as a disease-modifying agent specifically adapted to IVDD for repairing defects and AF without involving the use of exogenous stem cells. To treat AF rupture-induced IVDD, we here designed and developed T-MN. The IVD is the largest avascular organ in the human body, and its degeneration creates a hostile environment, which makes delivery of drugs challenging. Considering that AF has a tough structure, we used SilMA, a material with higher hardness, as the primary component and employed T-MN patches as drug delivery carriers that adhere to the ruptured AF and prevent NP extrusion. We employed 3D printing technology to design a threaded structure mold, which was used to manufacture the structure. The threaded structure enables a matching layered structure between T-MN and AF. On the one hand, T-MN increases the adhesion to AF. On the other hand, T-MN increases the area of drug release. Using our microneedle that matches the AF ring structure is more convenient and practical in clinical settings. It will inspire the development of disease-modifying therapies beneficial for IVDD patients. However, there are some limitations to our experiment, this research mainly evaluated disc degeneration at the radiological and histological levels and did not use biomechanical tests to test the function of the repaired IVD. The effect of exosomes-loading-T-MN on the biomechanics of disc degeneration needs further study.

The purpose of We here selected extracellular vesicles from BMSCs packed with miR-378 as the primary delivery drug for restoring AF mitophagy in IVDD, because miR-378 can restore mitophagy through the PDK-Akt pathway. Then, we used layer adhesive proteins as auxiliary materials to increase EXO@miR-378 adsorption and achieve sustained release *in vivo*. Compared with traditional IVDD treatment methods that primarily focus on NP repair, the treatment method proposed in our study focuses on AF rupture-induced IVDD, which has great clinical significance. In future, the microneedle formulation would be optimized for better therapeutic outcomes in large animal models before clinical applications, and its efficacy in other cartilage diseases would also be explored.

### 4. Conclusion

A new T-MN therapy system was developed that locks the defect site of AF *in situ* and delivers engineered exosomes@miR-378 for IVDD treatment. Our results demonstrate that the system can protect AF in IVDD by promoting AF cell proliferation and migration, inhibiting

pathological ECM remodeling, and restoring the mitophagy of AF cells. We believe that the current study results demonstrate the potential of microneedles with a special structure to deliver drugs for IVDD treatment.

### 5. Materials and methods

#### 5.1. Materials

Silk fibroin methacryloyl (SilMA, EFL-SilMA-001) and photoinitiator (lithium phenyl-2,4,6-trimethylbenzoylphosphine, LAP) were purchased from Suzhou Intelligent Manufacturing Research Institute, Suzhou, China. Laminin (derived from Engelbreth-Holm-Swarm basal membrane of mouse sarcoma) was acquired from Sigma Aldrich Company. PBS was from Qizhenhu Biological Technology Co., Ltd., Hangzhou, China.

#### 5.2. MN fabrication

**Solution preparation:** SilMA solutions of different concentrations were dissolved in PBS according to the mass volume ratio, and 0.5% (w/v) LAP was added. The solution was placed in a 50 °C water bath for 1 h to completely dissolve the solute. Next, laminin powder was added to the solution at a 10% (w/v) ratio. The SilMA-laminin mixture was obtained after complete dissolution.

**MN molding:** First, a resin male mold was printed using the projection-based printing (PBP) technique. The female mold was fabricated by casting PDMS into the male mold. Then, the SilMA-laminin mixture, prepared in advance, was poured into the PDMS mold and cured under UV light. To ensure the precise formation of the needle tip, vacuum was extracted several times when casting. When required, the dried MNs were soaked in the EXO suspension for several hours, removed, and freeze-dried again.

#### 5.3. Characterization and physical properties

**Fourier-transform infrared spectroscopy:** Freeze-dried SilMA was dissolved in PBS with 0.5% (w/v) LAP, and laminin powder was dissolved in pure PBS. The same steps were repeated, and then, the two solutions were mixed to obtain a mixture. Following UV photo cross-linking (20 mW/cm<sup>2</sup>) for 40 s to form the hydrogel, the sample was freeze-dried, ground, and mixed with KBr. The absorption peak of the sample was measured from 400 to 4000 cm<sup>-1</sup> by using an infrared spectrometer (Nicolet iS50).

**Scanning electron microscopy:** The internal structure and porosity of SilMA hydrogels prepared with different concentrations (10%, 15%, 20%, and 25% w/v) were observed through scanning electron microscopy. Briefly, a 5 × 5-mm hydrogel cylinder was prepared using a syringe tool and freeze-dried after UV photocrosslinking. The surface of the obtained sample was sprayed with gold, and observed and photographed under a scanning electron microscope (SU8010).

**Swelling test:** First, 5 × 5 mm (D × H) hydrogel cylinders with different concentrations were prepared as described above. After drying the sample overnight, it was weighed and the weight was recorded as W<sub>0</sub>. The sample was then placed in PBS solution at a bath ratio of 1:200 and removed at 10, 20, and 30 min and 24 h. The samples were weighed again at these respective time points, and the weights were recorded as W<sub>i</sub> (i = 10, 20, and 30 min and 24 h). The swelling ratio was calculated using the following formula:

**Tensile performance test:** Hydrogels with different concentrations were molded into standard parts. The tensile performance of the sample was determined on a universal testing machine (UTM2102) by applying a tensile force at a rate of 5 mm/min until the sample fractured. Based on the result obtained, a tensile stress-strain curve was drawn.

**Compression performance test:** First, 5 × 5 mm (D × H) hydrogel cylinders with different concentrations were prepared as described

above. Then, the compression performance of the sample was examined on the universal testing machine (UTM2102) by applying compression force at a rate of 1 mm/min until the sample fractured. A compressive stress–strain curve was drawn based on the result obtained.

**Tip strength test:** A  $3 \times 3$  MN array was prepared using the aforementioned method and placed on the platform with the tip facing upward. The tip strength of the needles was tested using the universal testing machine (UTM2102) at 0.5 mm/min until the needles fractured. A force–displacement curve was drawn based on the result obtained.

**Peeling adhesion test:** A  $10 \times 10$  MN array was prepared using the aforementioned method. The  $10 \times 10$  non-MN patch was prepared by pouring the SilMA hydrogel precursor into the mold without vacuuming, and therefore, the MN structure could not be formed. The tissue was fixed on the bottom plate, and the patch was fixed on the upper fixture plane. For the initial position, the MN patch's needles were inserted into the tissue or the non-MN patch was attached to the tissue. Then, the universal testing machine (UTM2102) was used to allow the fixture to move upward at 0.5 mm/min until the patch was removed from the tissue. A force–time curve was drawn based on the test result obtained.

#### 5.4. Isolation and identification of exosomes

BMSCs of Sprague–Dawley (SD) rats were purchased from Zhejiang Academy of Medical Sciences (Zhejiang, China). The cells were cultured in the corresponding growth medium (Raybiotech). Exosomes were extracted and purified from the BMSCs, as previously described. Briefly, the BMSC culture medium was collected every 24 h and centrifuged at 350 g for 10 min, followed by additional centrifugations for 10 min at 2000 g and then at 10,000 g for 30 min to remove the lifted cells and cell debris. Then, the supernatant was collected in an ultrafiltration tube (UFC9010, Millipore, Shanghai, China) and centrifuged at 3500 g for 10 min. The concentrated solution from the upper tube was collected and filtered through a 0.2- $\mu$ m pore membrane filter. The supernatant was ultracentrifuged at 100,000 g for 70 min at 4 °C by using a 70Ti rotor (BeckmanCoulter). The liquid in the centrifuge tube was carefully removed while an equal amount of PBS was added.

Finally, the supernatant was removed through centrifugation at 10,000 g for 90 min, and 5  $\mu$ L of PBS was added to collect the exosomes. The obtained exosomes were stored at  $-80$  °C. The exosome-related proteins, TSG101, calnexin and CD81 were analyzed through western blotting by using anti-TSG101 (ab125011, 1:1000, Abcam), anti-calnexin (ab133615, 1:1000, Abcam) and anti-CD81 (ab219209, 1:1000, Abcam) as primary antibodies. A ZetaView PMX 110 (Particle Metrix, Germany) was used for the NTA (nanometer size) analysis of the exosome samples. ZetaView 8.04.02 SP2 was used for analyzing the results. The exosome samples were observed using a JEM-1400 instrument (JEOL, Japan). We validated the characterization of exosomes. The purpose of loading miR-378 was achieved by using the ultrasonic shock method, using the power ultrasound of 250w, shaking for 2 s and stopping for 2 s, and the alternating cycle lasted for 10 min.

#### 5.5. Cell culture

Briefly, the AF tissue was carefully removed from the disc of 8-week-old SD rats ( $n = 2$ ). Then, the obtained tissue was cut into a paste and digested with 0.1% collagenase I (Gibco, Shanghai, China) at 37 °C for 40 min. Dulbecco's modified Eagle's medium (DMEM/F-12 (Gibco) was used to stop digestion. The mixture was then centrifuged at 1000 g for 5 min. Primary culture was obtained using DMEM/F12 in a humidified incubator at 37 °C under 5% CO<sub>2</sub>. 1 ml DMEM/F12 medium was added every other day for 7 days. Then the medium was changed every other day, and passaging was performed when the cell density was 80%. The third generation of AF cells was used in subsequent experiments with 5 nM IL-1 $\beta$  was added into medium for 24 h to degenerate AF cells.

#### 5.6. Immunofluorescence

AF cells were fixed on 24-well plates with 4% paraformaldehyde for 15 min and washed three times with PBS. Then, 0.2% Triton X-100 (W/V) in PBS was added to the cells for 15 min. After the cells were again washed three times with PBS, they were blocked with 5% bovine serum albumin (BSA) for 30 min.

Primary antibodies against ROS (E004-1-1, Nanjing Jiangcheng), MMP13 (ab315267, 1:100, Abcam, American), type I collagen (ab138492, 1:100; Novus, Abcam, American), or PI Calixanthin (1:100, Proteintech, China) were added followed by incubation at 4 °C for 12 h. Then, the secondary antibody [Alexa Fluor 555-labeled goat anti-rabbit IgG (1:500, Beyotime, China) or goat anti-rabbit Alexa Fluor 488 (1:500, Beyotime, China)] was added for incubation for 1 h. The images were captured with a fluorescence microscope (Leica).

#### 5.7. Western blotting

The proteins were extracted from cell samples by moderate-strength RIPA buffer supplemented with a proteasome inhibitor (BOSTER, China). Then, the proteins were separated using 10% SDS-PAGE and transferred onto the gel to a polyvinylidene fluoride membrane (Millipore, Shanghai, China). The membranes were subsequently blocked with 10% skimmed milk for an hour and washed with Tris-buffered saline with 0.1% Tween-20 (TBST) thrice. Anti-MMP13 (ab219620, Abcam, China), anti p62 (ab109012, Abcam), Anti-PDK1 (DF4365, Affinity, China), Anti-phospho-Akt (AF6261, Affinity, China), Anti-Akt (AF0016, Affinity, China), Anti-mTORC1 (AF3308, Affinity, China), Anti-ULK1 (AF4387, Affinity, China), Anti-FoxO1 (AF3417, Affinity, China), and Anti-FoxO3 (AF3020, Affinity, China) or anti-Col I (ab254360, Abcam, China) for 12 h. The internal control was anti  $\beta$ -actin (ab8227, Abcam). After washing away, the excess antibodies with TBST, and the membranes were incubated with specific horseradish peroxidase-conjugated secondary antibodies (Beyotime, China) at room temperature for 1 h. The immunoreactive bands were observed with a ChemiDocTouch imaging system (BioRad) to measure the signal intensity.

#### 5.8. Animal surgery

Male SD rats ( $n = 48$ , 250–270 g) were purchased from Shanghai Slack Laboratory Animal Company, Ltd. (China). The study was approved by local authorities (Zhejiang University affiliated secondary Medical University Laboratory Animal Research Center, China). The rats were anesthetized with 1% pentobarbital sodium (P-010, Merck, China) at a dose of 4 mL/kg. Then, the intervertebral spaces of coccygeal vertebrae [1]: control group (without surgery) [2]; injured group (with surgery) [3]; T-MN group (with surgery and fitting of T-MN) [4]; T-MN<sup>@EXO</sup> group (with surgery and fitting of T-MN<sup>@EXO</sup>); and [5] T-MN<sup>@EXO@miR-378</sup> group (with surgery and fitting of T-MN<sup>@EXO@378</sup>). We located the third and fourth coccygeal discs were located counting the vertebrae from the sacral region. Then, we cut the skin under a microscope at the dorsal midpoint of the caudal vertebrae with a #11 blade, avoiding damage to the blood vessels and bluntly separating the muscle until the outer AF was exposed. The disc was punctured with a 26-gauge sterile needle, in a parallel direction to the endplates. The needle was rotated at 360° and held in that position for 30s, while the full layers of the AF were damaged. And for mice, the tail IVDs Cy 5/6, 6/7, and 7/8 were exposed in each animal. A 0.5  $\times$  0.5 mm defect, approximately 0.4-mm deep was operated on each mouse.

#### 5.9. Disc height measurement

A molybdenum target (MCR-6000, China) was used to obtain X-ray images of the IVDs at 4 and 8 weeks. ImageJ (National Institute of

Health, USA) was employed for IVD height measurement.

Histological and immunohistochemical (IHC) analyses of the IVDs were performed. The caudal vertebrae of the rats were harvested at 4 and 8 weeks. The samples were fixed in 4% paraformaldehyde for 24 h and decalcified using 10% EDTA for 14 days (Booster, China). Once decalcification was complete, the tissues were dehydrated and embedded in paraffin. The paraffin specimen was cut into 5- $\mu$ m sections.

#### 5.10. Safranin O-fast green staining and immunohistochemical staining

Safranin O-fast green (SO) staining was performed to assess the degree of IVDD in each group. The average gray value (staining intensity) was used to grade the SO results, High positive (gray value181-236), Positive (gray value121-180), Low Positive (gray value61-120) and Negative (gray value0-60). And we grade each group as: Control group (High positive), Injured group (Low Positive), T-MN group (Low Positive), T-MN@EXO group (Positive), and T-MN@EXO@miR-378group (Positive). Col I and Fundc1 were used as immunohistochemical indicators of the degree of IVDD. The samples were treated with H<sub>2</sub>O<sub>2</sub> (3%) for 10 min, blocked with 5% BSA for 30 min at room temperature, and hybridized with Col I antibody (ab254360, 1:100; Affinity, China) or Fundc1 antibody (ab224722, 1:100; Abcam) or MMP13 antibody (ab219620, 1:100; Abcam) or Parkin (AF0235, 1:100; Affinity, China) or PINK1 (DF7742 1:100; Affinity, China) at 4 °C overnight. The samples were then washed five times with PBS and incubated with a biotin-labeled secondary antibody at 37 °C for 30 min. The SABC method was used to detect staining.

#### 5.11. Statistical analysis

All experiments were performed on at least three individual samples. \* $P < 0.05$  was considered to indicate a significant difference. The Shapiro–Wilk Normality test (Prism 8.0, GraphPad Software) was used to assess the normality of the data. Normally distributed data sets are presented as the means  $\pm$  standard deviation. Data sets were not normally distributed and expressed as the median value, and the Wilcoxon test or Kruskal–Wallis test was used to assess the statistical significance.

#### Funding statement

This work was supported by the National Natural Science Foundation of China (grant No. 81972514, 32371412 and 32071349), Zhejiang Provincial Natural Science Foundation of China under Grant No. LY23H060008 and LY24C100001, and National Health Commission Scientific Research Fund & Zhejiang Provincial Medical and Health Major Science and Technology Plan Project: WKJ-ZJ-2428.

#### Data availability statement

The original contributions presented in the study are included in the supplementary material, and further inquiries can be directed to the corresponding authors.

#### Ethics approval statement

All animal experiments were undertaken following a robust ethical review and in accordance with the procedures authorized by the Animal Ethics Committee of the Second Affiliated Hospital of Zhejiang University School of Medicine. the ethics certification was No.2023-121.

#### Patient consent statement

Not applicable.

#### Permission to reproduce material from other sources

Not applicable.

#### Clinical trial registration

Not applicable.

#### Declaration of competing interest

The authors declare that the research was conducted in the absence of any commercial or financial relationships that could be construed as a potential conflict of interest.

#### CRediT authorship contribution statement

**Shaojun Hu:** Writing – original draft, Conceptualization. **Meng Zhu:** Writing – original draft, Methodology. **Hongyuan Xing:** Conceptualization. **Yucheng Xue:** Methodology. **Jun Li:** Validation. **Zhan Wang:** Project administration. **Zhou Zhu:** Methodology. **Miaojie Fang:** Software. **Zilong Li:** Methodology. **Jianbin Xu:** Writing – review & editing, Funding acquisition. **Yong He:** Resources. **Ning Zhang:** Funding acquisition.

#### Acknowledgments

This work was supported by the National Natural Science Foundation of China (grant No. 81972514, 32371412 and 32071349), Zhejiang Provincial Natural Science Foundation of China under Grant No. LY23H060008 and LY24C100001, and National Health Commission Scientific Research Fund & Zhejiang Provincial Medical and Health Major Science and Technology Plan Project: WKJ-ZJ-2428.

#### Appendix A. Supplementary data

Supplementary data to this article can be found online at <https://doi.org/10.1016/j.bioactmat.2024.03.006>.

#### References

- [1] N.N. Knezevic, K.D. Candido, J.W.S. Vlaeyen, et al., Low back pain, *Lancet* 398 (10294) (2021) 78–92.
- [2] C. Maher, M. Underwood, R. Buchbinder, Non-specific low back pain, *Lancet* 389 (10070) (2017) 736–747.
- [3] Z. Zhou, S. Cui, J. Du, et al., One strike loading organ culture model to investigate the post-traumatic disc degenerative condition, *J. Orthop. Translat.* 26 (2021) 141–150.
- [4] I.L. Mohd Isa, S.L. Teoh, N.H. Mohd Nor, et al., Discogenic low back pain: anatomy, pathophysiology and treatments of intervertebral disc degeneration, *Int. J. Mol. Sci.* 24 (1) (2022).
- [5] A. Zhang, Z. Cheng, Y. Chen, et al., Emerging tissue engineering strategies for annulus fibrosus therapy, *Acta Biomater.* 167 (2023) 1–15.
- [6] E.J. Novais, V.A. Tran, S.N. Johnston, et al., Long-term treatment with senolytic drugs Dasatinib and Quercetin ameliorates age-dependent intervertebral disc degeneration in mice, *Nat. Commun.* 12 (1) (2021) 5213.
- [7] H. Xing, Z. Zhang, Q. Mao, et al., Injectable exosome-functionalized extracellular matrix hydrogel for metabolism balance and pyroptosis regulation in intervertebral disc degeneration, *J. Nanobiotechnol.* 19 (1) (2021) 264.
- [8] O.M. Torre, V. Mroz, M.K. Bartelstein, et al., Annulus fibrosus cell phenotypes in homeostasis and injury: implications for regenerative strategies, *Ann. N. Y. Acad. Sci.* 1442 (1) (2019) 61–78.
- [9] K. Sun, X. Jing, J. Guo, et al., Mitophagy in degenerative joint diseases, *Autophagy* 17 (9) (2021) 2082–2092.
- [10] Q. Wei, D. Liu, G. Chu, et al., TGF-beta1-supplemented decellularized annulus fibrosus matrix hydrogels promote annulus fibrosus repair, *Bioact. Mater.* 19 (2023) 581–593.
- [11] C.J. Panebianco, S. Rao, W.W. Hom, et al., Genipin-crosslinked fibrin seeded with oxidized alginate microbeads as a novel composite biomaterial strategy for intervertebral disc cell therapy, *Biomaterials* 287 (2022) 121641.
- [12] H. Chang, F. Cai, Y. Zhang, et al., Silencing gene-engineered injectable hydrogel microsphere for regulation of extracellular matrix metabolism balance, *Small Methods* 6 (4) (2022) e2101201.

- [13] S. Hu, H. Xing, J. Zhang, et al., Mesenchymal stem cell-derived extracellular vesicles: immunomodulatory effects and potential applications in intervertebral disc degeneration, *Stem Cell. Int.* 2022 (2022) 7538025.
- [14] R.D. Bowles, L.A. Setton, *Biomaterials for intervertebral disc regeneration and repair*, *Biomaterials* 129 (2017) 54–67.
- [15] Z. Wang, Y. Wu, Z. Zhao, et al., Study on transorgan regulation of intervertebral disc and extra-skeletal organs through exosomes derived from bone marrow mesenchymal stem cells, *Front. Cell Dev. Biol.* 9 (2021) 741183.
- [16] L. Xie, W. Huang, Z. Fang, et al., CircERC2 ameliorated intervertebral disc degeneration by regulating mitophagy and apoptosis through miR-182-5p/SIRT1 axis, *Cell Death Dis.* 10 (10) (2019) 751.
- [17] X. Yuan, T. Li, L. Shi, et al., Human umbilical cord mesenchymal stem cells deliver exogenous miR-26a-5p via exosomes to inhibit nucleus pulposus cell pyroptosis through METTL14/NLRP3, *Mol. Med.* 27 (1) (2021) 91.
- [18] Y. Huang, Z. Zhang, J. Wang, et al., circSPG21 protects against intervertebral disc disease by targeting miR-1197/ATP1B3, *Exp. Mol. Med.* 53 (10) (2021) 1547–1558.
- [19] Y. Zhao, A. Li, miR-19b-3p relieves intervertebral disc degeneration through modulating PTEN/PI3K/Akt/mTOR signaling pathway, *Aging (Albany NY)* 13 (18) (2021) 22459–22473.
- [20] Y. Li, J. Jiang, W. Liu, et al., microRNA-378 promotes autophagy and inhibits apoptosis in skeletal muscle, *Proc. Natl. Acad. Sci. U. S. A.* 115 (46) (2018) E10849–E10858.
- [21] L. Peng, Y. Chen, S. Shi, et al., Stem cell-derived and circulating exosomal microRNAs as new potential tools for diabetic nephropathy management, *Stem Cell Res. Ther.* 13 (1) (2022) 25.
- [22] C. He, S. Zheng, Y. Luo, et al., Exosome theranostics: biology and translational medicine, *Theranostics* 8 (1) (2018) 237–255.
- [23] L. Ying, C. Liang, Y. Zhang, et al., Enhancement of nucleus pulposus repair by glycoengineered adipose-derived mesenchymal cells, *Biomaterials* 283 (2022) 121463.
- [24] Y. Negishi, M. Nomizu, Laminin-derived peptides: applications in drug delivery systems for targeting, *Pharmacol. Ther.* 202 (2019) 91–97.
- [25] K. Tryggvason, The laminin family, *Curr. Opin. Cell Biol.* 5 (5) (1993) 877–882.
- [26] X. Li, Y. An, Q. Wang, et al., The new ceRNA crosstalk between mRNAs and miRNAs in intervertebral disc degeneration, *Front. Cell Dev. Biol.* 10 (2022) 1083983.
- [27] M. Chen, Z. Chen, Y. Wang, et al., Mitophagy receptor FUNDC1 regulates mitochondrial dynamics and mitophagy, *Autophagy* 12 (4) (2016) 689–702.
- [28] J. He, Y. Sun, Q. Gao, et al., Gelatin methacryloyl hydrogel, from standardization, performance, to biomedical application, *Adv. Healthcare Mater.* 12 (23) (2023) e2300395.
- [29] Z. Zhu, J. Wang, X. Pei, et al., Blue-ringed octopus-inspired microneedle patch for robust tissue surface adhesion and active injection drug delivery, *Sci. Adv.* 9 (25) (2023) eadh2213.
- [30] T. Waghule, G. Singhvi, S.K. Dubey, et al., Microneedles: a smart approach and increasing potential for transdermal drug delivery system, *Biomed. Pharmacother.* 109 (2019) 1249–1258.
- [31] D.B. Zorov, M. Juhaszova, S.J. Sollott, Mitochondrial reactive oxygen species (ROS) and ROS-induced ROS release, *Physiol. Rev.* 94 (3) (2014) 909–950.
- [32] T. Benzakour, V. Igoumenou, A.F. Mavrogenis, et al., Current concepts for lumbar disc herniation, *Int. Orthop.* 43 (4) (2019) 841–851.
- [33] S.M. Richardson, G. Kalamegam, P.N. Pushparaj, et al., Mesenchymal stem cells in regenerative medicine: focus on articular cartilage and intervertebral disc regeneration, *Methods* 99 (2016) 69–80.
- [34] S. Keshtkar, N. Azarpira, M.H. Ghahremani, Mesenchymal stem cell-derived extracellular vesicles: novel frontiers in regenerative medicine, *Stem Cell Res. Ther.* 9 (1) (2018) 63.
- [35] M. Saberi, X. Zhang, A. Mobasheri, Targeting mitochondrial dysfunction with small molecules in intervertebral disc aging and degeneration, *Geroscience* 43 (2) (2021) 517–537.